scientific reports

Check for updates

OPEN

Morphotype-based risk stratification in patients with patent foramen ovale using computational fluid dynamics

Fabio Morelli[1]✉, Valeria Guadagno[1], Tatiana Mencarini[1], Marta Brambilla[2], Laura Fusini[1,2], Silvia Bozzi[1], Daniela Trabattoni[2], Marina Camera[2,3]✉ & Alberto Redaelli[1]

Patent Foramen Ovale **(PFO) is a congenital cardiac anomaly, anatomically persistent in approximately 25% of the adult population. While traditionally associated with paradoxical embolism and cryptogenic stroke, increasing evidence suggests a functional link between PFO and migraine with aura. However, the biomechanical mechanisms underlying these associations remain poorly defined, particularly regarding the role of PFO morphology in modulating local hemodynamics and red blood cell (RBC) mechanical stress. This study employs computational fluid dynamics (CFD) combined with Lagrangian particle tracking to assess the impact of PFO tunnel geometry on flow behavior and RBC loading across eight representative morphologies. Velocity fields, wall shear stress (WSS), and particle-level stress histories were computed under physiologically calibrated boundary conditions replicating Valsalva-induced shunting. Results reveal a dichotomy between elongated/narrow and short/wide morphotypes, with the former exhibiting jet-like flows, higher WSS, and significantly elevated RBC stress metrics (up to 31 Pa and 0.49 Pa s of stress accumulation). The length-to-mean-quadratic-diameter ratio (L/D^2_{mean}) emerged as a strong predictor of mechanical exposure ($r = 0.98$), while outlet diameter correlated with potential systemic desaturation. This dual-scale analysis reveals a mechanistic connection between pathological stress levels and tunnel geometry, identifying L/D^2_{mean} as a candidate index for future imaging-based stratification of PFO-related clinical risk.**

Keywords Atrial Septal Defect, Particle Tracking, Morphometric Risk Predictor, Migraine with Aura, Cryptogenic Stroke, Red Blood Cells Scalar Stress

Patent foramen ovale (PFO) represents a persistent interatrial channel that results from the failure of complete anatomical fusion between the *septum primum* and *septum secundum* after birth. Its anatomical patency persists in approximately 25% of the adult population[1], rendering it one of the most prevalent congenital cardiac anomalies[2]. Despite its frequent incidental diagnosis, PFO has been associated with diverse clinical manifestations, ranging from paradoxical embolism to cryptogenic stroke[3–7].

Growing evidence also suggests a functional correlation between PFO and migraine with aura (MwA)[8], with several observational studies reporting symptom alleviation following percutaneous PFO closure[8–10], although the issue remains controversial. However, closure is currently recommended exclusively for secondary prevention in stroke-prone patients, and not for migraine management[11]. This discrepancy arises not only from a lack of mechanistic understanding linking PFO-mediated shunt physiology to neurovascular disturbances, but also from conflicting outcomes in randomized clinical trials[7,8]. While recent meta-analyses have suggested potential benefit of PFO closure in selected migraine patients[8,12], the overall evidence remains inconclusive, thereby limiting formal guideline recommendations[13–15]. Several pathophysiological hypotheses have been advanced to explain the neurovascular consequences of PFO, including paradoxical embolism, transit of vasoactive substances, arterial hypoxemia, and platelet activation mediated by oxidative stresss[12]. The latter has been recently demonstrated in the LEARNER study, where PFO-associated systemic stress was shown to enhance platelet activation in patients with migraine and aura[16]. Two further underexplored yet biologically

[1]Department of Electronics, Information and Bioengineering, Politecnico di Milano, Milan, Italy. [2]Centro Cardiologico Monzino IRCCS, Milan, Italy. [3]Department of Pharmaceutical Sciences, Università degli Studi di Milano, Milan, Italy. ✉email: fabio.morelli@polimi.it; Marina.Camera@cardiologicomonzino.it

plausible contributors are red blood cell (RBC) mechanotransduction under abnormal shear conditions, and the passage of deoxygenated blood to the systemic circulation without pulmonary filtration[17,18].

RBCs are known to respond to mechanical stress by releasing ATP, nitric oxide intermediates, and reactive oxygen species (ROS), all of which have been implicated in neurovascular activation and cortical spreading depression, a central event in the genesis of migraine with aura[19,20]. *In vivo* evidence from the LEARNER study further supports this hypothesis, reporting a mild yet significant reduction in RBC count and microvesicle release in patients with PFO, both of which normalized following device closure[21]. Notably, shear stresses in the "sub-hemolytic" range (10–60 Pa) have been shown to elicit such responses *in vitro*[17]. Simultaneously, elevated shunt volumes through PFOs have been associated with measurable drops in systemic arterial oxygen saturation (SaO_2), especially during positional maneuvers, potentially leading to cerebral hypoxia[18,22]. Despite these plausible links, the interplay between PFO morphology[23,24], hemodynamics, and RBC biomechanics remains insufficiently characterized. Current literature lacks a detailed, quantitative analysis of how anatomical variability in the PFO tunnel modulates blood flow patterns and cellular stress exposure[25,26].

The present study addresses this gap by investigating how variations in PFO channel geometry influence flow behavior and RBC stress levels, using high-resolution computational fluid dynamics (CFD) and particle-based Lagrangian tracking. Specifically, we quantify the stress levels experienced by red blood cells as they transit the PFO; we examine how morphological variability affects local flow features in terms of velocity profiles and wall shear stress (WSS); and we assess the volumetric shunt bypassing pulmonary circulation. Eventually, this work proposes morphotypes-based risk stratification grounded in clinically measurable PFO metrics, as obtained from intracardiac ultrasound imaging. These objectives are pursued through a methodological framework that couples CFD-derived velocity and shear stress fields with particle-based Lagrangian tracking to identify stress history of individual RBC trajectories. Accordingly, a dual-scale biomechanical analysis aims to propose new morphometric indices for risk stratification.

Materials and methods

Data collection

A retrospective analysis was conducted at the IRCCS Centro Cardiologico Monzino on a cohort of 31 patients diagnosed with patent foramen ovale. The diagnostic protocol employed transcranial contrast-enhanced Doppler ultrasonography (Dolphin/MAX TCD machine, Viasonix Ltd., Ra'Anana IL), incorporating microbubble injection concurrent with the Valsalva maneuver to confirm PFO patency. Subsequent interventions for PFO closure utilized intracardiac ultrasound-guided (ULTRA ICE™, Boston Scientific, Marlborough US) device implantation. During catheter-based procedures, the pressure in the atria was recorded during the Valsalva maneuver, allowing identification of the transient pressure drop associated with PFO opening. This value, representing the transatrial pressure gradient, was used to calibrate boundary conditions in the CFD simulations.

A systematic review of the literature was conducted to identify the most frequently reported morphological characteristics of patent foramen ovale, with particular focus on quantifiable geometric metrics (Fig. 1, Left Panel). Data were extracted from studies employing a variety of measurement techniques, including autopsy investigations[27], balloon catheter-based assessments[28,29], and transesophageal echocardiography (TEE)[30–34]. Six primary anatomical parameters emerged as recurrently reported: the length of the PFO channel (L), the inlet diameter (D_{in}), the outlet diameter (D_{out}), the angle between the septum primum and septum secundum (α), and the thicknesses of both septa (th_1 for septum primum, th_2 for septum secundum). Among these, the subset of L, D_{in}, and D_{out} was selected for quantitative modeling, given their prevalence and consistency across

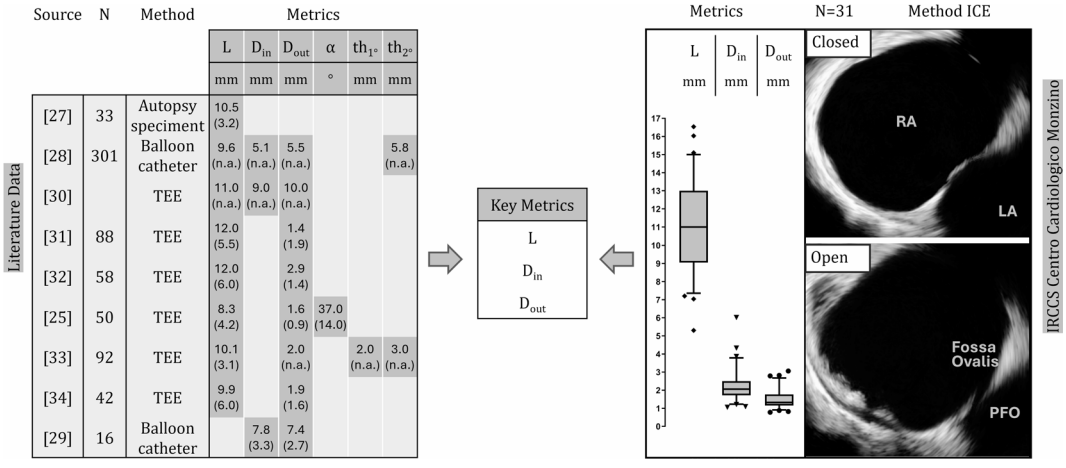

Fig. 1. Left Panel) Literature-derived synthesis of PFO morphologies. Reported metrics across multiple studies include channel length (L), inlet diameter (D_{in}), outlet diameter (D_{out}), interseptal angle (α), and septal thicknesses (th_1, th_2). Data were extracted from autopsy analyses[27], balloon catheter measurements[28,29], and transesophageal echocardiography (TEE) studies[30–34]. Right Panel) Patient-derived PFO geometries. Intracardiac echocardiographic images annotated to extract morphological parameters (L, D_{in}, D_{out}) used to parameterize virtual models.

studies. The aggregated values for these three parameters were averaged to define a reference patient geometry (Pat0).

In parallel, dynamic intracardiac echocardiographic (ICE) images were annotated by clinicians to extract quantitative morphometric parameters of the PFO, including channel length (L), inlet diameter (D_{in}), and outlet diameter (D_{out}) (Fig. 1, Right Panel). The absence of significant interdependence among the three morphological metrics in the cohort enabled the stratification of morphological variability. Eight representative cases were delineated, including three extreme configurations characterized by the maximum channel length, the minimum outlet diameter, and the maximum outlet diameter, respectively, along with four additional cases derived through stochastic sampling within the observed metric ranges (Table 1).

The study was conducted according to the Declaration of Helsinki, it was approved by the institutional Ethics Committee (n. CCM 1934, Comitato Etico degli IRCCS Istituto Europeo di Oncologia e Centro Cardiologico Monzino) and written informed consent was obtained from all participants.

Model development

Given the absence of high-resolution, segmentable imaging, a paradigmatic cardiac model developed by collaborating academic institutions[35] was employed as the foundation for constructing eight patient-specific geometries. This approach aimed to isolate the hemodynamic contributions of PFO morphology while maintaining anatomical consistency. Internal atrial and venous surfaces were extracted, whereas ventricular structures were omitted. The atrioventricular valves were modeled in the closed position to simulate atrial systole, the phase during which PFO-mediated flow occurs.

The fossa ovalis location was identified[27,30]. Within the SolidWorks CAD software environment, a simplified geometric conduit connecting the atria was constructed, comprising a cylindrical segment (fossa ovalis), a transitional region, and an inclined conical section representing the PFO channel. Dimensions were parameterized based on the extracted metrics (D_{in}, D_{out}, and L). Surface smoothing and coarse remeshing of all geometries were performed using Meshmixer. Subsequent refinement within the ANSA (BetaCAE) environment subdivided the models into 16 macroregions with variable triangular mesh densities. Three boundary layers with a growth rate of 1.1 were generated. The final tetrahedral volumetric mesh contained nine million elements. To verify mesh independence, simulations were conducted on three successively refined grids derived from the most geometrically irregular patient case. Refinement was applied by scaling the base element size while preserving a constant growth ratio. The variable used to assess convergence was the averaged pressure over the PFO inlet section. Richardson extrapolation and Grid Convergence Index (GCI) analysis were performed, and the selected mesh (9 million elements) yielded $< 5\%$ deviation from the finest mesh, confirming numerical reliability with acceptable computational cost[36]. Figure 2 exhibits the whole process of the model development.

CFD simulations

The mesh models were imported into Ansys Fluent for transient computational fluid dynamics simulations, conducted under the assumptions of rigid walls[37] and laminar flow (Reynolds number subsequently evaluated to verify this assumption). Blood was approximated as an incompressible Newtonian fluid (density: 1060 $\mathrm{kg/m^3}$; dynamic viscosity: 0.003 Pa s)[38]. The incompressible Navier–Stokes equations were solved in conservative form:

$$\nabla \cdot \mathrm{v} = 0 \tag{1}$$

$$\rho \left(\frac{\partial \mathrm{v}}{\partial t} + \mathrm{v} \cdot \nabla \mathrm{v} \right) = -\nabla p + \mu \nabla^2 \mathrm{v} \tag{2}$$

where v is the velocity vector, p the pressure, ρ the fluid density, and μ the dynamic viscosity.

Inflow partitioning within the right atrium was established based on literature values, allocating 65% of the total 5 L/min flow to the inferior vena cava (IVC) and 35% to the superior vena cava (SVC)[39,41–43]. For the left atrium, inflows were distributed among the four pulmonary veins in proportion to their respective cross-sectional areas[44,45]. A reference pressure was applied to one pulmonary vein to ensure numerical stability.

To account for atrial compliance without resorting to a full fluid-structure interaction (FSI) framework, outflow boundary conditions were imposed on the atrial walls, implemented as Neumann conditions (zero

	Pat0	Pat1	Pat2	Pat3	Pat4	Pat5	Pat6	Pat7
Features	Mean Literature	D_{outmin} (M)	D_{outmax} (M)	L_{max} (M)	Sampled (Monzino)	Sampled (Monzino)	Sampled (Monzino)	Sampled (Monzino)
L [mm]	10.16	9.60	14.60	16.03	10.72	9.19	8.65	12.18
D_{in} [mm]	5.24	1.22	3.40	2.50	5.42	5.60	2.56	3.32
D_{out} [mm]	3.63	0.78	3.06	1.26	2.52	2.38	1.23	2.81

Table 1. Geometric parameters used for the eight PFO models included in the analysis. We selected a set of configurations to ensure representative anatomical variability. Pat0 corresponds to averaged morphometric values obtained from literature. Pat1 to Pat3 are patient-specific geometries extracted from clinical data provided by Centro Cardiologico Monzino, representing the minimum D_{out}, maximum D_{out}, and maximum L patient, respectively. Pat4 to Pat7 were synthetically generated using stochastic sampling within the observed dimensional ranges, in the absence of significant correlation among the three primary metrics (L, D_{in}, D_{out}), to comprehensively explore the parameter space.

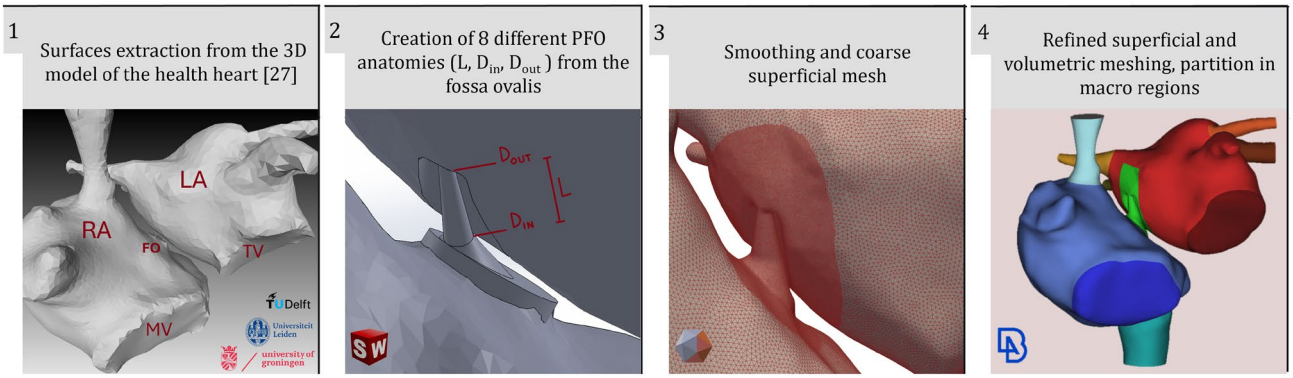

Fig. 2. Workflow for atrial geometry reconstruction and PFO model parametrization. (1) Internal surfaces of the atria, venous inlets, and atrioventricular valves (closed configuration) were extracted from a high-resolution anatomical model developed by TU Delft, Leiden University, and University of Groningen. The fossa ovalis was identified to define the PFO insertion site. (2) A simplified interatrial conduit representing the PFO was created in SolidWorks, composed of a cylindrical and a conical segment. Eight variants were generated by varying inlet diameter (D_{in}), outlet diameter (D_{out}), and channel length (L). (3) Surface smoothing and coarse remeshing were performed to ensure topological consistency. (4) The geometry was volumetrically meshed in ANSA with tetrahedral elements, three boundary layers (growth rate 1.1), and partitioned into macroregions for boundary condition assignment.

gradient) on all three velocity components, as described by Redaelli et al. (2004) [37]. This configuration mimics atrial expansion during late systole and prevents the entire venous inflow from being forced through the PFO (Fig. S1). Flow balancing between the atria was ensured using the following equations:

$$Q_{\text{out–R}} = \sum Q_{\text{in–R}} - Q_{\text{PFO}} \tag{3}$$

$$Q_{\text{out–L}} = \sum Q_{\text{in–L}} + Q_{\text{PFO}} \tag{4}$$

$$\sum Q_{\text{in–L}} = \sum Q_{\text{in–R}} = 5\,\frac{l}{\text{min}} \tag{5}$$

The magnitude of this outflow was iteratively tuned to replicate the physiological interatrial pressure gradient measured during catheterized Valsalva maneuvers ($\Delta P = 4$ mmHg). Although this method assumes spatially uniform atrial dilation, it allows for a realistic division of flow between atrial expansion and trans-PFO shunting.

Simulations utilized the PISO algorithm for pressure-velocity coupling, with first-order discretization for pressure and second-order Upwind schemes for momentum equations. A second-order implicit temporal discretization scheme was employed with a timestep of 0.0001 s (Courant number < 1), ensuring solution convergence within 300 iterations at a residual threshold of 1×10^{-4}. Mechanical stress on red blood cells (RBCs) was assessed by simulating the motion of spherical particles through the PFO tunnel and quantifying the stresses acting along their trajectories. To this end, approximately 30000 rigid, non-deformable particles with a diameter of 8 μm, representative of RBCs, were released from the IVC and SVC inlet surfaces, with one particle injected from the centroid of each surface mesh cell to ensure uniform spatial coverage. Particle trajectories were computed by integrating the force balance equation using the Discrete Phase Model (DPM). For low-inertia particles such as RBCs, the dominant force is the drag exerted by the surrounding fluid. This equation was solved for each particle by numerically integrating its motion over time using a Lagrangian framework superimposed on the Eulerian fluid field, under the one-way coupling assumption (i.e., no influence of particle motion on the fluid flow). A rebound condition was imposed for particles impacting the vessel walls. Simulations continued until all particles exited through a hemispherical surface surrounding the fossa ovalis, which defined the outlet of the PFO shunt.

Metrics

The Eulerian approach was employed to compute volumetric velocity fields and wall shear stress distributions within the PFO region, facilitating inter-patient comparisons of hemodynamic variability. The volumetric flow rate Q through a surface A was calculated as:

$$Q = \int_A \mathrm{v} \cdot \mathrm{n}\, dA \tag{6}$$

All quantities were extracted from the final, stabilized state of the transient simulation. The shear vector was computed by *Fluent* as the viscous shear force per unit area acting at the wall, defined as:

$$\boldsymbol{\tau}_w = \mu\left(\nabla \mathrm{v} + \nabla \mathrm{v}^T\right) \cdot \mathrm{n} - \left[\mu\left(\nabla \mathrm{v} + \nabla \mathrm{v}^T\right) \cdot \mathrm{n} \cdot \mathrm{n}\right] \mathrm{n} \tag{7}$$

where n is the unit normal vector to the wall. The scalar wall shear stress (WSS) was extracted as the magnitude $|\boldsymbol{\tau}_w|$ of the shear vector.

Lagrangian particle tracking simulations, conducted within Fluent, incorporated a user-defined function to calculate the scalar stress (SS) for each particle at each time step, following the formulation by Apel et al[46].:

$$SS = \frac{1}{\sqrt{3}}\sqrt{\sigma_{11}^2 + \sigma_{22}^2 + \sigma_{33}^2 - \sigma_{11}\sigma_{22} - \sigma_{11}\sigma_{33} - \sigma_{22}\sigma_{33} + 3\left(\tau_{12}^2 + \tau_{13}^2 + \tau_{23}^2\right)} \tag{8}$$

where σ_{ii} are the normal stresses and τ_{ij} are the shear components of the Cauchy stress tensor. The scalar stress is an invariant measure of the local deviatoric stress and is commonly used to estimate the mechanical load that would be experienced by deformable particles such as red blood cells in reality, although they are modeled here as rigid tracers in a continuum-based CFD framework[47,48]. Postprocessing in MATLAB involved the extraction of particle trajectories at planes located 4 mm upstream and downstream of the PFO. Scalar stress vs. time curves were smoothed using LOESS filtering and uniformly resampled. Derived metrics included positive shear stress loading rate (SR^+), negative shear stress loading rate (SR^-), and stress accumulation, computed as follows[49]:

$$SR^+ = \frac{1}{n^+}\sum_{i=1}^{n^+-1}\frac{|SS_{i+1} - SS_i|}{\Delta t} \tag{9}$$

$$SR^- = \frac{1}{n^-}\sum_{i=1}^{n^--1}\frac{|SS_{i+1} - SS_i|}{\Delta t} \tag{10}$$

$$SA = \sum_{i=1}^{n-1}\frac{SS_i + SS_{i+1}}{2}\Delta t \tag{11}$$

where n^+ and n^- are the number of intervals with positive and negative scalar stress slopes, respectively, and SS_i is the instantaneous scalar stress at time t_i. Comparative analysis of these metrics across cases was visualized in terms of median values and 5$^{\text{th}}$ and 95$^{\text{th}}$ percentile.

Results

Hemodynamic metrics' analysis

The computational fluid dynamics simulations performed on eight distinct patient-specific PFO geometries enabled the quantification of trans-PFO volumetric blood flow (Q_{PFO}), ensuring that boundary conditions replicated the *in vivo* interatrial pressure gradient. As expected, Q_{PFO} constitutes a minor fraction of total cardiac output (CO), exhibiting substantial variability in Q_{PFO} across morphological phenotypes. Figure 3 reports the flow rates through the 8 PFO geometries with values ranging from 0.015 L/min (0.3% CO) in Pat1 to 0.60 L/min (12% CO) in Pat0. Intermediate values were observed in Pat2, Pat4, and Pat7 (0.30 L/min).

Absolute flow rates were lowest in elongated and constricted PFO morphologies manifesting elevated hydraulic resistance, as seen in Pat1 and Pat3. While configurations with a wider cross-sectional area, such as Pat0 and Pat2, exhibited comparatively higher Q_{PFO} values. Figure 3 shows the velocity vector fields and the WSS contour maps for the eight analyzed cases. The velocity vector maps are shown in a representative cross-sectional area of the PFO channel. Data reveal substantial inter-morphological divergence in peak velocity ($V_{\max}$), with recorded values spanning from 0.80 m/s (Pat6) to 2.70 m/s (Pat1). The distal PFO egress, located between the septum primum and septum secundum, consistently coincided with the site of peak velocity in all morphologies. The comparison of velocity magnitudes highlights that an elongated and narrow channel morphology promotes a jet-like outflow regime with increased velocity peaks. This is most prominent in Pat1 and Pat3, where $V_{\max}$ attains values exceeding threefold those of shorter, broader PFO geometries. Reynolds numbers computed at the PFO outlet, where flow velocity and geometric constriction are maximal, remained well below the transitional threshold ($\mathrm{Re} < 2300$) in all cases, supporting the validity of the laminar flow assumption.

The right panels of Fig. 3 depict the spatial distribution of wall shear stress, revealing peak shear concentrations at the distal exit of the PFO channel, consistent with velocity maxima loci. The maximum WSS ($\mathrm{WSS}_{\max}$) exhibits considerable inter-morphological variability, with recorded values ranging from 25 Pa (Pat2) to 106 Pa (Pat1). Notably, elongated and narrow PFOs (Pat1, Pat3) display severe localized shear stress amplification, while shorter, wider channels attenuate WSS magnitudes.

Correlation analysis between morphological determinants and hemodynamic metrics

To quantitatively assess the impact of PFO morphology on hemodynamics, a morphometric stratification approach was introduced (Table 2). By combining the three initial parameters (D_{in}, D_{out}, and Length), the following metrics were extracted and analyzed: length-to-mean-quadratic-diameter ratio (L/D_{mean}^2), length-to-mean-diameter ratio (L/D_{mean}), length-to-outlet-quadratic-diameter ratio (L/D_{out}^2), length-to-outlet-diameter ratio (L/D_{out}), conicity ($D_{\mathrm{out}}/D_{\mathrm{in}}$) and convergence ($L/|D_{\mathrm{out}} - D_{\mathrm{in}}|$). Among the extracted metrics, the length-to-mean-quadratic-diameter ratio (L/D_{mean}^2) was identified as a key descriptor for classification:

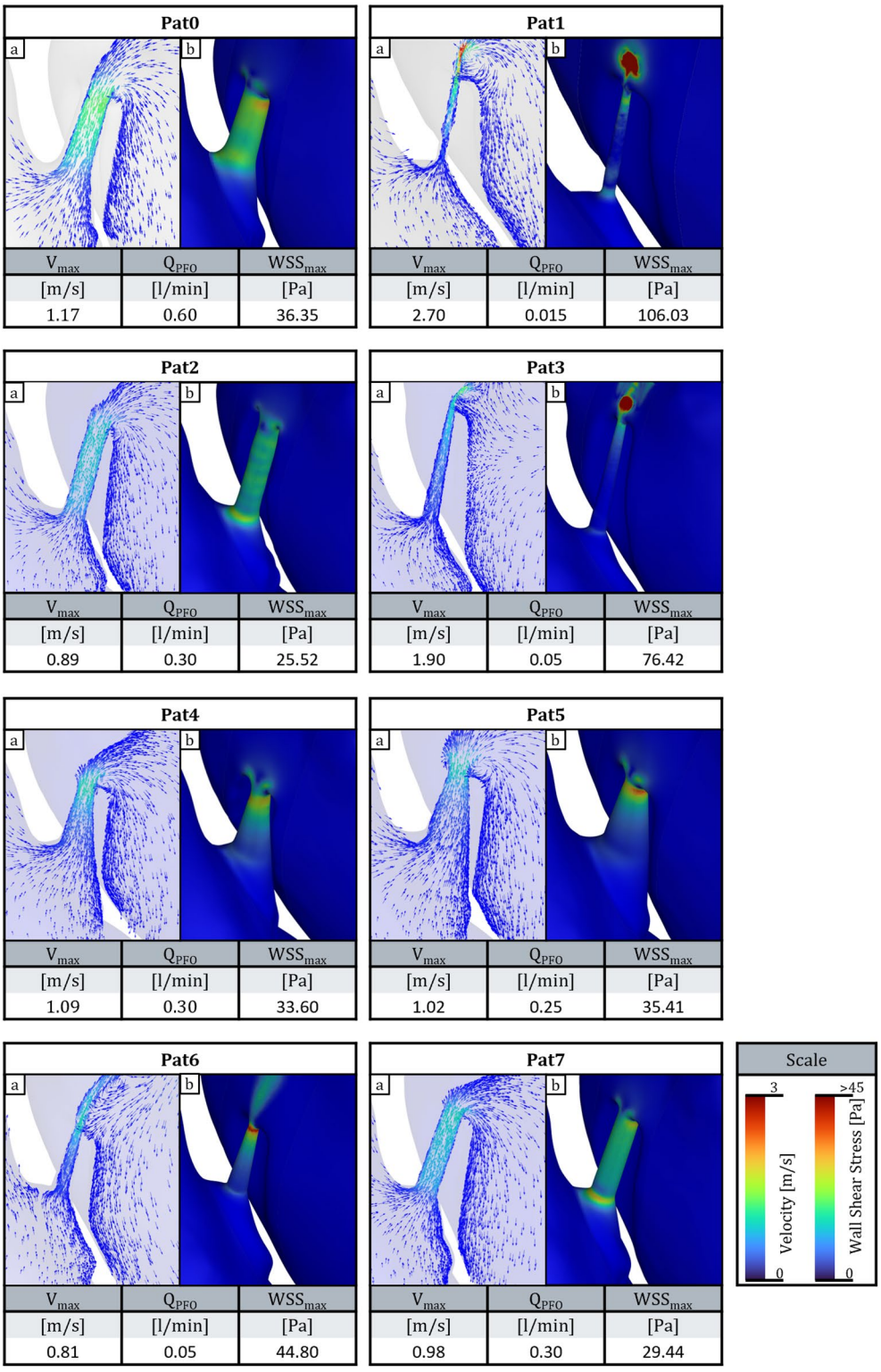

Fig. 3. Velocity vector maps and identification of high wall shear stress (WSS) zones from CFD on eight PFO geometries. For each morphology, the left panel ("a") illustrates the velocity vectors within the PFO, highlighting inter-morphological variability in peak velocity magnitudes, ranging from 0.80 m/s in broad, short configurations (Pat6) to 2.70 m/s in elongated, narrow geometries (Pat1). The right panel ("b") displays the spatial distribution of WSS, revealing peak values localized at the distal PFO outflow region, coinciding with high-velocity jet emergence. The $WSS_{\max}$ magnitude in Pat1 and Pat3 is threefold and twofold higher, respectively, compared to all other cases. The respective Q_{PFO} values are also reported.

	V_{max}	WSS_{max}	Q_{PFO}
D_{in}	-0.61	-0.72	0.75
D_{out}	-0.64	-0.81	0.95
Length	0.08	0.00	-0.06
L/D_{mean}^2	0.93	0.96	-0.70
L/D_{mean}	0.86	0.90	-0.76
L/D_{out}^2	0.91	0.98	-0.77
L/D_{in}	0.83	0.86	-0.69
Conicity (D_{out}/D_{in})	-0.10	-0.23	0.36
Divergence ($L/\|D_{out}-D_{in}\|$)	0.08	0.00	-0.07

Table 2. Correlation between morphometric indices and hemodynamic parameters extracted from CFD. Both peak velocity within the PFO and WSS_{max} exhibit strong positive correlations with the derived length-to-mean-quadratic-diameter ratio (L/D_{mean}^2). Similar relationships are observed when using the length-to-outlet-quadratic-diameter metric, reinforcing the role of tunnel constriction in shaping intrachannel flow characteristics. Additionally, outlet diameter correlates strongly with Q_{PFO}, suggesting a primary role in governing trans-PFO blood transport. Pearson correlation coefficients are reported.

- $L/D_{mean}^2 > 3 \rightarrow$ Elongated and narrow morphologies (e.g., Pat1, Pat3) are associated with significantly higher peak velocities and WSS_{max}, indicative of a stenotic flow regime and localized shear stress concentration.
- $L/D_{mean}^2 < 3 \rightarrow$ Shorter and wider PFOs (e.g., Pat0, Pat2, Pat6) exhibit lower velocity gradients and WSS values, corresponding to a flow behavior closer to physiological conditions.

A Pearson correlation analysis confirmed the strong relationship between L/D_{mean}^2 and hemodynamic parameters, with correlation coefficients of $r = 0.93$ for peak velocity and $r = 0.96$ for maximum WSS (Table 2). On the other hand, Q_{PFO} exhibited a strong correlation ($r = 0.95$) with the PFO outlet diameter, indicating that a narrower D_{out} is the predominant factor constraining the volumetric flow rate through the PFO channel. This relationship underscores the critical role of outlet morphology in modulating trans-PFO hemodynamics.

RBC stress metrics' analysis

Particle-tracking simulations (e.g., Video S1, Video S2, representative of the two distinct morphology-driven flow patterns) confirmed that blood flow through the PFO originates from both the inferior and superior vena cava, without preferential inlet dominance. The streamlines' contour in the top-left panel of Fig.4 distinctly delineates the concurrent contribution of both atrial inlets to the trans-PFO blood flow. Qualitative analysis of particle-tracking simulations revealed a consistent preferential pathway near the upper PFO wall, with morphology-dependent differences in transit velocity and dispersion, indicating the impact of anatomical variation on flow organization. These features are exemplified by two representative cases, Pat3 and Pat6, shown in Supplementary Videos S1 and Video S2, respectively. A detailed Lagrangian assessment of RBC mechanical loading revealed substantial inter-patient variability across all evaluated stress metrics, including maximum scalar stress, peak shear stress loading rate, cumulative stress accumulation, and mean shear stress loading rate (subdivided into positive and negative components). This variability closely mirrored the trends observed in hemodynamic parameters. As illustrated in Fig. 4, among the analyzed geometries, Pat1 and Pat3, characterized by elongated and constricted PFO tunnels, exhibited the highest mechanical stress values. The median maximum scalar stress reached 24 Pa in Pat1 and 31 Pa in Pat3, whereas in all other morphologies, it remained confined within the 1–3 Pa range. A similar trend was observed for the maximum shear stress loading rate, with median values of 349 Pa/s and 438 Pa/s in Pat1 and Pat3, respectively, compared to 44–172 Pa/s in the remaining geometries.

Morphological determinants of RBC stress metrics

The correlation analysis between morphometric indices and RBC mechanical loading parameters, as derived from particle-tracking simulations, revealed a strong association (Table 3). Specifically, the length-to-mean-quadratic-diameter ratio exhibited a robust correlation with stress accumulation ($r = 0.98$) and RBC residence time ($r = 0.92$), further quantifying the morphology-dependent variation in RBC exposure to mechanical forces.

Discussion

This computational study offers a comprehensive analysis of the hemodynamic and mechanical implications arising from anatomical variability in patent foramen ovale morphology. The results, derived from transient CFD simulations and Lagrangian particle tracking across eight representative geometries, reveal a substantial modulation of both flow rate and red blood cell stress in relation to PFO structural parameters. Two distinct morphotypic profiles, elongated and narrow versus short and wide, emerged as functionally divergent, reflecting opposing hemodynamic regimes with potential pathophysiological relevance.

To our knowledge, this is the first study to systematically investigate the role of PFO morphology in shaping intrachannel hemodynamics and RBC-level mechanical loading. Prior works have analyzed general atrial flow patterns or shunt dynamics, but none have directly integrated morphological indices with both macroscopic

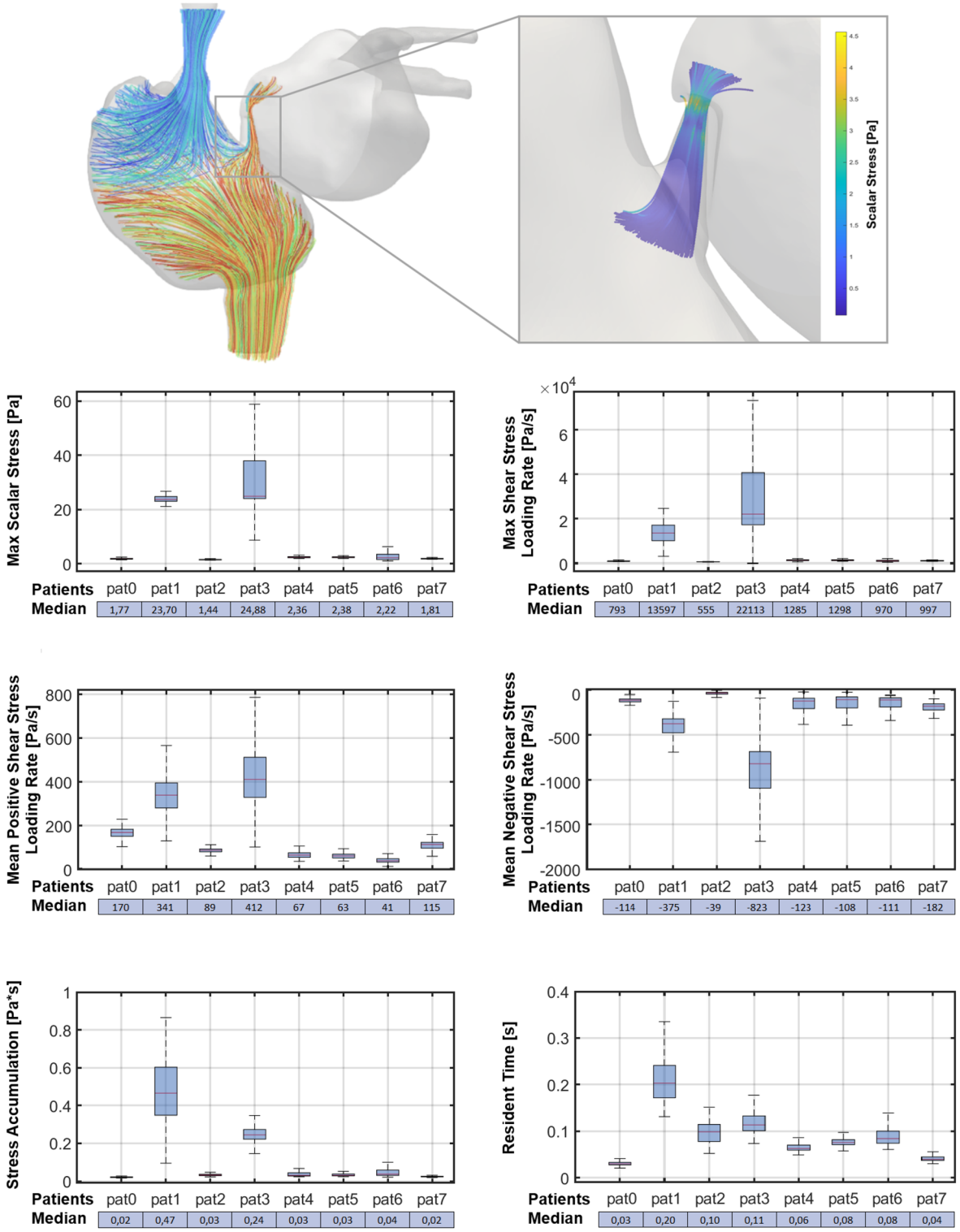

Fig. 4. Mechanical loading history of red blood cells (RBCs) transiting through the eight PFO morphologies. RBCs from both atrial inlets, without preferential dominance, undergo markedly different stress magnitudes depending on PFO anatomy. Pat1 and Pat3 manifest maximum scalar stress values of 24 Pa and 30 Pa, respectively, whereas other morphologies remain within the unit range. Stress accumulation (*SA*), quantifying cumulative mechanical load along RBC trajectories, reaches median values of 0.49 Pa s (Pat1) and 0.27 Pa s (Pat3), versus 0.02–0.05 Pa s in the others. Boxplots illustrate median, interquartile range, and 5th–95th percentiles.

Correlation	Max Scalar Stress	Max Shear Stress Loading Rate	Mean Pos Shear Stress Loading Rate	Mean Neg Shear Stress Loading Rate	Stress Accumulation	Resident Time
L/D^2_{mean}	0.80	0.74	-0.57	0.65	0.98	0.92
L/D_{mean}	0.91	0.85	-0.76	0.83	0.93	0.89
L/D^2_{out}	0.87	0.78	-0.68	0.75	0.97	0.91
L/D_{in}	0.85	0.81	-0.67	0.75	0.91	0.87
Conicity ($D_{\text{out}}/D_{\text{in}}$)	-0.22	-0.05	0.31	-0.24	-0.10	-0.10
Divergence ($L/\lvert D_{\text{out}} - D_{\text{in}}\rvert$)	0.05	0.10	0.09	0.01	0.17	0.31

Table 3. Correlation between morphometric indices and RBC stress metrics. The length-to-mean-quadratic-diameter ratio (L/D^2_{mean}) shows strongest correlation with stress accumulation ($r = 0.98$) and RBC residence time ($r = 0.92$), highlighting the role of tunnel elongation in modulating RBC exposure. Similar trends are seen for all length-to-diameter ratios (L/D_{mean}, L/D^2_{out}, L/D_{in}). Maximum scalar stress correlates strongly with all morphometric indices, except Conicity and Divergence. Pearson correlation coefficients are reported.

flow descriptors and microscale RBC stress. In this context, the introduction of the metric L/D^2_{mean} enabled a consistent, geometry-based classification of PFO morphotypes with predictive value for flow patterns and shear stress behavior. Notably, similar trends were observed with the metric L/D^2_{out}, which also showed strong correlation with peak velocity and WSS. Both formulations include squared diameter in the denominator, effectively capturing the influence of cross-sectional area. While diameter-based forms were preferred in reporting due to direct measurability in clinical imaging (ICE), the relation aligns with physical expectations: stress increases with narrowing length and decreases with the cross-sectional area ($\propto 1/D^2$).

The volumetric flow rate (Q_{PFO}) was primarily governed by outlet diameter (D_{out}), with a Pearson correlation of $r = 0.95$. Wider morphologies such as Pat0 and Pat2 supported substantial shunt volumes (0.60 and 0.30 L/min), whereas elongated, narrow channels (Pat1 and Pat3) exhibited lower flow, consistent with increased hydraulic resistance. In contrast, peak velocity (V_{max}) and (WSS_{max}) were most strongly correlated with L/D^2_{mean}, with $r = 0.93$ and 0.96 respectively. Geometries with $L/D^2_{\text{mean}} > 3$ consistently generated jet-like, stenotic flow characterized by high velocity gradients and shear amplification, particularly at the distal exit.

The integration of Lagrangian particle tracking allowed cell-specific stress analysis, adding an unprecedented layer of detail to the mechanical characterization of PFO transit. In high L/D^2_{mean} morphologies, RBCs were exposed to scalar stress levels between 24–31 Pa, with cumulative stress accumulation up to 0.49 Pa s: values markedly higher than those observed in short, wide geometries (<3 Pa and <0.05 Pa s). These magnitudes fall within the "sub-hemolytic" range (10–60 Pa) reported in literature to induce membrane deformation, ATP release, and oxidative stress responses without full lysis[17,19,50]. Such stimuli have been linked to endothelial activation and cortical spreading depression, suggesting a possible mechanistic pathway for migraine with aura[17]. Full hemolytic thresholds (>150 Pa) were not reached, reinforcing the relevance of non-destructive but biologically active mechanical exposures[17]. Additionally, residence time within the channel was significantly prolonged in elongated morphotypes, with a Pearson correlation of $r = 0.92$ versus L/D^2_{mean}. The combination of high shear and prolonged exposure likely enhances mechanotransduction potential and may support the hypothesis of RBC stress–mediated neurovascular activation. Systemic consequences of PFO morphology were also considered from an oxygenation perspective. Clinical literature identifies right-to-left shunt volumes >0.4–0.5 L/min as sufficient to induce transient arterial desaturation, with reported SaO_2 drops of 88–92%[22,51]. In this study, Pat0 surpassed this critical threshold, while Pat2 approached it. The relevance of this hypoxia depends on additional factors, such as PFO channel opening frequency, pulmonary reserve, and compensatory cerebral vasodilation, that were not modeled here. Nonetheless, elevated shunt volumes remain a plausible contributor to symptoms, particularly for migraine with aura[18].

A critical interpretive question concerns whether the primary pathogenic driver is high mechanical stress or high unoxygenated flow. The current data do not fully resolve this dichotomy. Elevated Q_{PFO} may facilitate paradoxical embolism or allow neuroactive venous metabolites to bypass pulmonary clearance[18]. In contrast, high shear and stress accumulation, as observed in narrow and elongated channels, may elicit RBC-mediated signaling with direct neurovascular effects. These mechanisms are not mutually exclusive and may be differentially expressed across PFO morphotypes. A preliminary clinical correlation supporting this hypothesis emerges from OCT-based findings by Yan et al[52]., where PFOs in stroke patients showed a trend toward smaller diameters and increased lengths compared to controls ($p = 0.08$ and $p = 0.16$, respectively). This morphological profile mirrors the "narrow and elongated" configurations identified in our study as generating maximal RBC stress. While not statistically conclusive, these data suggest that geometrical characteristics may outweigh shunt flow rate in determining risk, reinforcing the rationale for stress-focused, morphology-based classifiers such as L/D^2_{mean}.

The strong correlation between L/D^2_{mean} and stress-related metrics supports its candidacy as a risk stratification marker. Morphotypes exceeding a threshold of $L/D^2_{\text{mean}} > 3$ consistently presented high-velocity jets, localized WSS peaks, and elevated RBC stress, suggesting a morphologically grounded biomechanical risk. While the clinical utility of such a parameter requires prospective validation, it offers a mechanistically supported, imaging-accessible criterion for identifying high-risk PFOs. In parallel, risk stratification from an oxygenation

perspective may benefit from identifying a threshold in D_{out}, given its strong correlation with Q_{PFO} ($r = 0.95$). In the present study, PFO morphologies with $D_{\mathrm{out}} > 3.5$ mm consistently produced Q_{PFO} values near or above the 0.5 L/min threshold, which has been associated with arterial desaturation in previous studies. While further clinical validation is warranted, this D_{out} threshold value may serve as an imaging-accessible discriminator of desaturation risk and may provide an actionable anatomical criterion alongside L/D^2_{mean}.

The methodology adopted in this study introduces several strengths. The dual approach, combining classical CFD descriptors with individual particle histories, enables a comprehensive view of both bulk flow behavior and microscopic mechanical exposure. This represents a significant step beyond traditional CFD analyses, bridging macrofluid dynamics and cellular mechanobiology. On the other hand, the morphometric stratification enables direct mapping between imaging-accessible parameters and mechanical risk profiles, supporting translational applicability in clinical contexts.

Despite its strengths, the study includes some simplifying assumptions. The model does not explicitly include atrial wall motion; nonetheless, atrial expansion was indirectly incorporated by imposing a normal outflow on the left atrial surface, tuned to replicate the transatrial pressure drop measured in vivo. This approach, as previously adopted within our group[37], provides a reasonable approximation of atrial compliance, although it does not fully capture localized wall parameters such as regional curvature and tissue-specific stiffness. Moreover, in this context, wall deformability plays a role upstream, by modulating the portion of flow directed into the PFO, but does not directly impact the intra-channel hemodynamics. Regarding the PFO structure, it can be reasonably modeled as rigid due to the fibrous composition and low compliance of the interatrial septum[27]. Thus, while more advanced computational frameworks may account for regional tissue elasticity, the present approach, anchored to physiological pressure conditions, offers a rational balance between complexity and mechanistic fidelity, and is not expected to compromise the validity of the proposed L/D^2_{mean} risk threshold.

Furthermore, blood was modeled as a Newtonian fluid, which constitutes a simplification of its shear-thinning nature. However, the impact of non-Newtonian rheology has been shown to depend more on the nature of the flow than on fixed shear rate thresholds. In flow regimes characterized by well-organized streamlines (such as confined jets, stenoses, or tunnel-like conduits) differences between Newtonian and non-Newtonian models become negligible for hemodynamic quantities like WSS and scalar stress. In this context, the Newtonian approximation is considered appropriate[38]. RBCs were represented as rigid tracers, and no deformation dynamics were explicitly modeled. This simplification excludes the potential influence of viscoelastic response or membrane fatigue. However, the scalar stress invariant, as defined in this study, accounts for the full deviatoric component of the local stress tensor and it captures the magnitude of mechanical load that would act on a deformable particle, providing a physically relevant surrogate for estimating mechanobiological stimuli. This approximation has been widely adopted in previous studies investigating blood element mechanobiology in continuum-based CFD models[47,48]. Moreover, no direct *in vivo* validation is yet available to link modeled stress exposure with cellular dysfunction. In this perspective, microfluidic platforms may represent a powerful validation tool to replicate the mechanical loading histories derived from simulation. The cumulative scalar stress and velocity profiles identified here may serve as input constraints for the design of microfluidic platforms that emulate PFO-like geometries. These platforms allow controlled in vitro experiments (e.g., RBC activation assays, flow cytometry, or oxidative stress quantification) to evaluate functional alterations under defined shear conditions. This coupling of computational and experimental frameworks has been successfully implemented in previous studies[49,53,55,56]. This would allow direct translation of fluid dynamic simulations into biomolecular readouts, extending the utility of CFD beyond mechanical metrics into the field of cell function and pathophysiology.

Studies investigating adult PFO hemodynamics remain rare, mainly due to the difficulty of deriving models from standard clinical imaging, such as echocardiography. To our knowledge, only one study has been published combining anatomical modeling of the PFO with flow dynamics computational analysis[57], but the simulations are limited to qualitative flow visualization and focus on exploring potential links with atrial fibrillation, without in-depth hemodynamic quantification or morphotype-driven interpretation. As a result, current risk stratification in adults predominantly relies on clinical scoring systems such as RoPE[14,58] and PASCAL[59,60], which integrate demographic, symptomatic, and qualitative imaging features. The present work complements these approaches by introducing a morphology-based, simulation-driven framework capable of quantifying local mechanical conditions that may predispose to red blood cell damage or paradoxical embolism, thus providing a novel mechanistic layer to existing risk assessment paradigms. To enhance translational applicability, we further synthesized the two proposed morphometric indices into a two-dimensional risk stratification matrix (Fig. 5). Each analyzed case is mapped within this framework according to their L/D^2_{mean} and D_{out} values, surrogate markers for mechanical and desaturation risk, respectively. This graphical representation highlights the relative position of each case with respect to the proposed thresholds and may serve as a visual decision-support tool. Such geometric indices can be extracted from standard imaging modalities, potentially integrating into clinical workflows to inform closure decisions. It should be noted, however, that the threshold values currently proposed are derived from a limited sample size. Future investigations with larger and more heterogeneous populations are warranted to refine and validate these cut-off values for broader clinical adoption.

In conclusion, this study establishes a foundational link between PFO morphology, local hemodynamic alterations, and RBC-relevant mechanical stress. The results support a mechanistic model in which anatomical variations modulate not only flow volume but also the character and intensity of mechanical stimuli experienced by RBCs. While high flow and systemic hypoxia remain clinically relevant, the consistently elevated mechanical stress observed in narrow, elongated channels underscores the potential role of PFO morphodynamics in triggering neurological symptoms. The analytical approach presented here lays the groundwork for future biomimetic validation and opens new insight for morphotype-based clinical decision-making in the management of PFO-related syndromes.

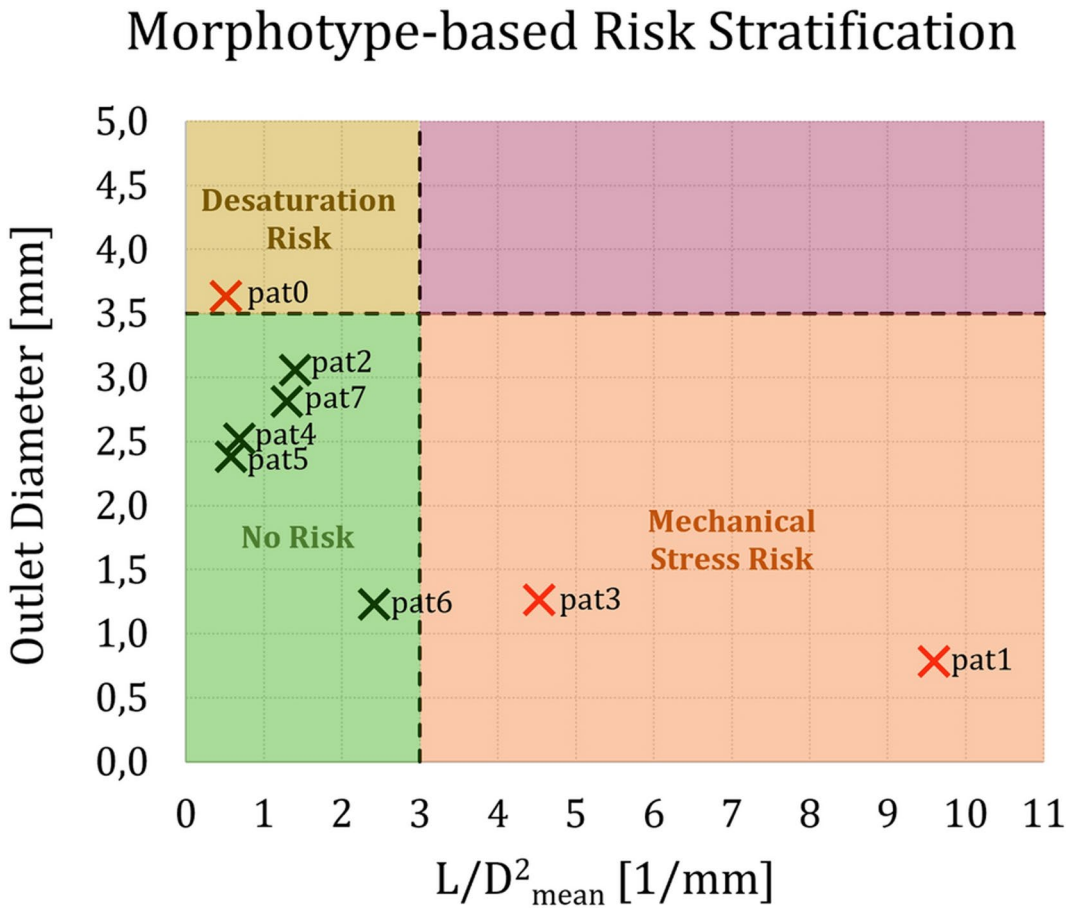

Fig. 5. Morphotype-based risk stratification matrix. Each marker corresponds to one of the eight analyzed PFO morphologies, plotted according to the two proposed morphometric indices (L/D^2_{mean} and D_{out}). Dashed lines indicate the threshold values associated with elevated risk of mechanical loading and desaturation. Red markers represent morphotypes that exceed at least one risk threshold, while green markers fall within the low-risk region. This graphical classification tool provides an intuitive overview of PFO-related risk and could support clinical decision-making regarding patient monitoring and closure indication.

Data availability

The data that support the findings of this study are available from corresponding author on reasonable request.

Received: 26 May 2025; Accepted: 28 August 2025
Published online: 03 October 2025

References

1. Hagen, P. T., Scholz, D. G. & Edwards, W. D. Incidence and size of patent foramen ovale during the first 10 decades of life: an autopsy study of 965 normal hearts. *Mayo Clin. Proc.* **59**, 17–20. https://doi.org/10.1016/S0025-6196(12)60336-X (1984).
2. Koutroulou, I. et al. Epidemiology of patent foramen ovale in general population and in stroke patients: A narrative review. *Front. Neurol.* **11**, 281. https://doi.org/10.3389/fneur.2020.00281 (2020).
3. Webster, M. W. et al. Patent foramen ovale in young stroke patients. *Lancet* **2**, 11–12. https://doi.org/10.1016/S0140-6736(88)92944-3 (1988).
4. Overell, J. R., Bone, I. & Lees, K. R. Interatrial septal abnormalities and stroke: a meta-analysis of case-control studies. *Neurology* **55**, 1172–1179. https://doi.org/10.1212/WNL.55.8.1172 (2000).
5. Di Tullio, M. R., Sacco, R. L., Gopal, A., Mohr, J. P. & Homma, S. Patent foramen ovale as a risk factor for cryptogenic stroke. *Annals Intern. Medicine* **117**, 461–465. https://doi.org/10.7326/0003-4819-117-6-461 (1992).
6. Kim, J. S. Patent foramen ovale and other cardiopathies as causes of embolic stroke with unknown source. *J. Stroke* **26**, 349–359. https://doi.org/10.5853/jos.2024.02670 (2024).
7. Amini, T. Cryptogenic stroke and patent foramen ovale: endeavoring for clarity. *Front. Neurol.* **15**, 1533232. https://doi.org/10.3389/fneur.2024.153323 (2025).
8. Silalahi, T. D. A. & Hariyanto, T. I. Efficacy and safety of patent foramen ovale closure for mitigating migraine: a systematic review and meta-analysis of randomized trials and observational studies. *Ther. Adv. Neurol. Disord.* **17**, 17562864241271032. https://doi.org/10.1177/17562864241271033 (2024).
9. Tobis, J. M. et al. Percutaneous closure of patent foramen ovale in patients with migraine: the premium trial. *J. Am. Coll. Cardiol.* **70**, 2766–2774. https://doi.org/10.1016/j.jacc.2017.09.1105 (2017).
10. Saver, J. L. et al. Long-term outcomes of patent foramen ovale closure or medical therapy after stroke. *New Engl. J. Medicine* **377**, 1022–1032. https://doi.org/10.1056/NEJMoa1610057 (2017).

11. Sposato, L. A., Albin, C. S. W., Elkind, M. S. V., Kamel, H. & Saver, J. L. Patent foramen ovale management for secondary stroke prevention: State-of-the-art appraisal of current evidence. *Stroke* **55**, 236–247. https://doi.org/10.1161/STROKEAHA.123.040546 (2024).
12. Rigatelli, G. et al. Primary transcatheter patent foramen ovale closure is effective in improving migraine in patients with high-risk anatomic and functional characteristics for paradoxical embolism. *JACC: Cardiovasc. Interv.* **3**, 282–287. https://doi.org/10.1016/j.jcin.2009.11.019 (2010).
13. Lip, P. Z. & Lip, G. Y. Patent foramen ovale and migraine attacks: a systematic review. *The American journal of medicine* **127**, 411–420. https://doi.org/10.1016/j.amjmed.2013.12.006 (2014).
14. Kent, D. M. et al. An index to identify stroke-related vs incidental patent foramen ovale in cryptogenic stroke. *Neurology* **81**, 619–625. https://doi.org/10.1212/WNL.0b013e3182a08d59 (2013).
15. Kleindorfer, D. O. et al. 2021 guideline for the prevention of stroke in patients with stroke and transient ischemic attack: A guideline from the american heart association/american stroke association. *Stroke* **52**, e364–e467. https://doi.org/10.1161/STR.0000000000000375 (2021).
16. Trabattoni, D. et al. Migraine in patients undergoing pfo closure: characterization of a platelet-associated pathophysiological mechanism: the learner study. *Basic to Transl. Sci.* **7**, 525–540. https://doi.org/10.1016/j.jacbts.2022.02.002 (2022).
17. Horobin, J. T., Sabapathy, S. & Simmonds, M. J. Red blood cell tolerance to shear stress above and below the subhemolytic threshold. *Biomech. Model. Mechanobiol.* **19**, 851–860. https://doi.org/10.1007/s10237-019-01252-z (2020).
18. Blanche, C. et al. Platypnea-orthodeoxia syndrome in the elderly treated by percutaneous patent foramen ovale closure: a case series and literature review. *Eur. J. Intern. Medicine* **24**, 813–817. https://doi.org/10.1016/j.ejim.2013.08.698 (2013).
19. Buerck, J. P. et al. Production of erythrocyte microparticles in a sub-hemolytic environment. *J. Artif. Organs* **24**, 135–145. https://doi.org/10.1007/s10047-020-01231-7 (2021).
20. Sprague, R. S., Ellsworth, M. L., Stephenson, A. H. & Lonigro, A. J. Participation of camp in a signal-transduction pathway relating erythrocyte deformation to atp release. *Am. J. Physiol. Physiol.* **281**, C1158–C1164. https://doi.org/10.1152/ajpcell.2001.281.4.C1158 (2001).
21. Camera, M. et al. Patent foramen ovale (pfo) and migraine: role of platelet tissue factor expression and oxidative stress. the learner study. *Eur. Hear. J.* **43**, ehac544–1835, https://doi.org/10.1093/eurheartj/ehac544.1835 (2022).
22. Godart, F. et al. Atrial right-to-left shunting causing severe hypoxaemia despite normal right-sided pressures. report of 11 consecutive cases corrected by percutaneous closure. *Eur. heart journal* **21**, 483–489. https://doi.org/10.1053/euhj.1999.1944 (2000).
23. Yetiş Sayın, B. & Oto, A. Patent foramen ovale: A practical and imaging based morphological classification. *J Updat. Cardiovasc. Med* **10**, 47–56. https://doi.org/10.32596/ejcm.galenos.2022.2022-05-032 (2022).
24. Tian, J. & Chen, X. Pfo morphology for evaluation of c-tcd and c-tte rls grades. *Eur. J. Med. Res.* **27**, 228. https://doi.org/10.1186/s40001-022-00855-0 (2022).
25. Nakayama, R. et al. Identification of high-risk patent foramen ovale associated with cryptogenic stroke: development of a scoring system. *J. Am. Soc. Echocardiogr.* **32**, 811–816. https://doi.org/10.1016/j.echo.2019.03.021 (2019).
26. Rigatelli, G., Zuin, M. & Roncon, L. Increased blood residence time as markers of high-risk patent foramen ovale. *Transl. Stroke Res.* **14**, 304–310. https://doi.org/10.1007/s12975-022-01045-0 (2023).
27. Klimek-Piotrowska, W., Hołda, M., Koziej, M., Piątek, K. & Hołda, J. Anatomy of the true interatrial septum for transseptal access to the left atrium. *Annals Anat. - Anat. Anzeiger* **205**, https://doi.org/10.1016/j.aanat.2016.01.009 (2016).
28. Sorensen, S. G., Spruance, S. L., Smout, R. & Horn, S. Transcranial doppler quantification of residual shunt after percutaneous patent foramen ovale closure: correlation of device efficacy with intracardiac anatomic measures.. *journal of interventional cardiology* **25**, 304–312. https://doi.org/10.1111/j.1540-8183.2011.00714.x (2012).
29. Spence, M. S., Khan, A. A. & Mullen, M. J. Balloon assessment of patent foramen ovale morphology and the modification of tunnels using a balloon detunnelisation technique. *Catheter Cardiovasc Interv.* **71**, 222–228. https://doi.org/10.1002/ccd.21415 (2008).
30. Rana, B. S., Shapiro, L. M., McCarthy, K. P. & Ho, S. Y. Three-dimensional imaging of the atrial septum and patent foramen ovale anatomy: defining the morphological phenotypes of patent foramen ovale. *Eur. J. Echocardiogr.* **11**, i19–i25. https://doi.org/10.1093/ejechocard/jeq122 (2010).
31. Komar, M. et al. Transoesophageal echocardiography can help distinguish between patients with "symptomatic" and "asymptomatic" patent foramen ovale. *Kardiologia polska* **70**, 1258–1263 (2012).
32. Goel, S. S. et al. Morphology of the patent foramen ovale in asymptomatic versus symptomatic (stroke or transient ischemic attack) patients. *Am. J. Cardiol.* **103**, 124–129. https://doi.org/10.1016/j.amjcard.2008.08.036 (2009).
33. Nermin, B. et al. Assessment of morphology of patent foramen ovale with transesophageal echocardiography in symptomatic and asymptomatic patients. *J. Stroke Cerebrovasc. Dis.* **24**, 1282–1286. https://doi.org/10.1016/j.jstrokecerebrovasdis.2015.01.036 (2015).
34. Natanzon, A. & Goldman, M. E. Patent foramen ovale: anatomy versus pathophysiology–which determines stroke risk?. *J. Am. Soc. Echocardiogr.* **16**, 71–76. https://doi.org/10.1067/mje.2003.34 (2003).
35. de Goeje L. et al. Atrial septal defect (asd). *Sketchfab* https://skfb.ly/6RAH8 (2019).
36. Phillips, T. S. & Roy, C. J. Richardson extrapolation-based discretization uncertainty estimation for computational fluid dynamics. *J. Fluids Eng.* **136**, https://doi.org/10.1115/1.4028020 (2014).
37. Redaelli, A. et al. Flow dynamics of the st jude medical symmetry aortic connector vein graft anastomosis do not contribute to the risk of acute thrombosis. *The J. Thorac. Cardiovasc. Surg.* **128**, 117–123. https://doi.org/10.1016/j.jtcvs.2004.02.039 (2004).
38. Arzani, A. Accounting for residence-time in blood rheology models: do we really need non-newtonian blood flow modelling in large arteries? *J. Royal Soc. Interface,* **15**, https://doi.org/10.1098/rsif.2018.0486. (2018).
39. Parker, L. P., Svensson Marcial, A., Brismar, T. B., Broman, L. M. & Prahl Wittberg, L. Impact of altered vena cava flow rates on right atrium flow characteristics. *J. applied physiology* **132**, 1167–1178. https://doi.org/10.1152/japplphysiol.00649.2021 (2022).
40. Cohen, M. L., Cohen, B. S., Kronzon, I., Lighty, G. W. & Winer, H. E. Superior vena caval blood flow velocities in adults: a doppler echocardiographic study. *J. applied physiology* **61**, 215–219. https://doi.org/10.1152/jappl.1986.61.1.215 (1986).
41. Wexler, L., Bergel, D. H., Gabe, I. T., Makin, G. S. & Mills, C. J. Velocity of blood flow in normal human venae cavae. *Circ. research* **23**, 349–359. https://doi.org/10.1161/01.res.23.3.349 (1968).
42. Yalonetsky, S., Tal, R., Aharonson, D., Gross, G. & Lorber, A. Superior vena cava-right atrium junction flow-pattern post-transcatheter closure of patent foramen ovale. *Echocardiography* **36**, 1698–1700. https://doi.org/10.1111/echo.14448 (2019).
43. Huaxia, P. et al. The exploration of flow pattern in the superior vena cava of healthy adults: A 4d flow magnetic resonance imaging study. *Medicine Nov. Technol. Devices* **18**, https://doi.org/10.1016/j.medntd.2023.100232 (2023).
44. Lantz, J. et al. Impact of pulmonary venous inflow on cardiac flow simulations: Comparison with in vivo 4d flow mri. *Annals of biomedical engineering* **47**, 413–424. https://doi.org/10.1007/s10439-018-02153-5 (2019).
45. Basnight, M. A., Gonzalez, M. S., Kershenovich, S. C. & Appleton, C. P. Pulmonary venous flow velocity: relation to hemodynamics, mitral flow velocity and left atrial volume, and ejection fraction. *J. Am. Soc. Echocardiogr.* **4**, 547–558. https://doi.org/10.1016/s0894-7317(14)80213-7 (1991).
46. Apel, J., Paul, R., Klaus, S., Siess, T. & Reul, H. Assessment of hemolysis related quantities in a microaxial blood pump by computational fluid dynamics. *Artif. organs* **25**, 341–347. https://doi.org/10.1046/j.1525-1594.2001.025005341.x (2001).

47. Arora, D., Behr, M. & Pasquali, M. A tensor-based measure for estimating blood damage. *Artif. organs* **28**, 1002–1015. https://doi.org/10.1111/j.1525-1594.2004.00072.x (2004).
48. Grigioni, M., Morbiducci, U., D'Avenio, G., Benedetto, G. D. & Del Gaudio, C. A novel formulation for blood trauma prediction by a modified power-law mathematical model. *Biomech. modeling mechanobiology* **4**, 249–260. https://doi.org/10.1007/s10237-005-0005-y (2005).
49. Consolo, F. et al. High frequency components of hemodynamic shear stress profiles are a major determinant of shear-mediated platelet activation in therapeutic blood recirculating devices. *Scientific Reports* **7**, https://doi.org/10.1038/s41598-017-05130-5 (2017).
50. Simmonds, M. J. & Meiselman, H. J. Prediction of the level and duration of shear stress exposure that induces subhemolytic damage to erythrocytes. *Biorheology* **53**, 237–249. https://doi.org/10.3233/BIR-16120 (2016).
51. Devuyst, G. et al. Controlled contrast transcranial doppler and arterial blood gas analysis to quantify shunt through patent foramen ovale. *Stroke* **35**, 859–863. https://doi.org/10.1161/01.STR.0000119384.28376.EB (2004).
52. Yan, C. & Li, H. Preliminary investigation of in situ thrombus within patent foramen ovale in patients with and without stroke. *JAMA* **325**, 20. https://doi.org/10.1001/jama.2021.4359 (2021).
53. Dimasi, A. et al. Microfluidic flow-based platforms for induction and analysis of dynamic shear-mediated platelet activation–initial validation versus the standardized hemodynamic shearing device. *Biomicrofluidics* **12**, 042208. https://doi.org/10.1063/1.5024500 (2018).
54. Bluestein, D., Yin, W., Affeld, K. & Jesty, J. Flow-induced platelet activation in mechanical heart valves. *The J. heart valve disease* **13**, 501–508 (2004).
55. Dimasi, A. et al. Microfluidic emulation of mechanical circulatory support device shear-mediated platelet activation. *Biomed. Microdevices* **17**, https://doi.org/10.1007/s10544-015-0015-1 (2015).
56. Valerio, L. et al. Shear-mediated platelet activation in patients implanted with continuous flow lvads: A preliminary study utilizing the platelet activity state (pas) assay. *Annu. Int. Conf. IEEE Eng. Medicine Biol. Soc.* 1255–1258, https://doi.org/10.1109/EMBC.2015.7318595 (2015).
57. Rigatelli, G., Zuin, M., Dell'Avvocata, F. & Roncon, L. Computational flow dynamic analysis of right and left atria in patent foramen ovale: Potential links with atrial fibrillation. *J. Atr. Fibrillation* **10**, 1852. https://doi.org/10.4022/jafib.1852 (2018).
58. Kent, D. M. et al. Risk of paradoxical embolism (rope)-estimated attributable fraction correlates with the benefit of patent foramen ovale closure: An analysis of 3 trials. *Stroke* **51**, 3119–3123. https://doi.org/10.1161/STROKEAHA.120.029350 (2020).
59. Kent, D. M. et al. Evaluating therapies to prevent future stroke in patients with patent foramen ovale-related strokes —the scope study. Patient-Centered Outcomes Research Institute (PCORI), https://doi.org/10.25302/04.2023.RS.SCOPE2019001 (2023).
60. Lee, O. H. & Kim, J. S. Percutaneous patent foramen ovale closure after stroke. *Korean Circ. J.* **52**, 801–807. https://doi.org/10.4070/kcj.2022.0258 (2022).

Acknowledgements

The authors gratefully acknowledge funding from Project CUP B43C22001110008 - PNRR-MAD-2022-12376277 - PNRR-M6C2I2.1 NextGenerationEU and PNC E3- 2022-23683266 - Advanced diagnosis (HLS-DA) "INNO-VA".

Author contributions

F.M. developed the computational models, conducted the CFD simulations, performed the data analysis and results interpretation, wrote the original draft and implemented the revisions requested by the reviewers. V.G. contributed to the conceptual development, supported preliminary analyses, and assisted in interpreting the results. T.M. contributed to result interpretation. L.F. and D.T. collected clinical images and patient data, and supported the interpretation of clinical implications. M.B., A.B. and M.C. coordinated clinical collaboration and reviewed the manuscript. S.B. and A.R. supervised the research and critically revised the manuscript. M.C. and A.R. conceived the study and secured project funding. All authors reviewed and approved the final version of the manuscript.

Declarations

Competing interests

The authors declare no competing interests.

Additional information

Supplementary Information The online version contains supplementary material available at https://doi.org/10.1038/s41598-025-17926-x.

Correspondence and requests for materials should be addressed to F.M. or M.C.